Synthesis and characterization of mesoporous α-Fe$_2$O$_3$ nanoparticles and investigation of electrical properties of fabricated thick films

Ali Mirzaei[1,*], Kamal Janghorban[1], Babak Hashemi[1], Seyyed Reza Hosseini[1], Maryam Bonyani[1], Salvatore Gianluca Leonardi[2], Anna Bonavita[1], Giovanni Neri[2]

[1]*Department of Materials Science and Engineering, Shiraz University, Shiraz, Iran*
[2]*Department of Electronic Engineering, Chemistry and Materials Engineering, University of Messina, Italy*

Abstract

In this work, α-Fe$_2$O$_3$ nanoparticles (NPs) have been synthesized by using a simple Pechini sol-gel method from iron nitrate, citric acid as complexing agent and ethylene glycol as polymerization agent. The calcined α-Fe$_2$O$_3$ NPs were fully characterized by different techniques. It was confirmed that ultrafine and highly crystalline α-Fe$_2$O$_3$ NPs with high purity and mesoporous nature can be obtained after calcination at 550 °C for 3 h. In addition, the results of electrical resistance measurements of the fabricated Fe$_2$O$_3$ thick films showed that α-Fe$_2$O$_3$ thick films have stable electrical properties which are beneficial for electrical applications such as gas sensing and field effect transistors.

Keywords: α-Fe$_2$O$_3$, Pechini sol-gel, structural characterization, electrical resistance

I. Introduction

Iron (III) oxides have been one of the most extensively investigated transition metal oxides. Besides the amorphous phase, Fe$_2$O$_3$ has four polymorphs: i) α-Fe$_2$O$_3$; ii) β-Fe$_2$O$_3$; iii) γ-Fe$_2$O$_3$; and iv) ε-Fe$_2$O$_3$. While the highly crystalline α-Fe$_2$O$_3$ and γ-Fe$_2$O$_3$ occur in nature, β-Fe$_2$O$_3$ and ε-Fe$_2$O$_3$ are generally synthesized in the laboratory [1]. Each polymorph possesses peculiar crystal structures and physical properties, i.e. electrical, optical, and photoelectrical. Among them hematite (α-Fe$_2$O$_3$) has many peculiar properties, such as low precursor and synthesis cost, low toxicity, abundance, environmental friendly nature, easy production and storage, high corrosion resistance, chemical inertness, biocompatibility and excellent substrate adherence [2,3]. These features make α-Fe$_2$O$_3$ very interesting for researchers and have led to intense investigation of this material for applications in many areas such as water treatment [4], contrast reagents/drug delivery [5], sensor technology [6,7], optical coatings, magnetic materials [8], field effect transistor [9], catalysts [10], pigments [11], etc. As a consequence, various

α-Fe$_2$O$_3$ crystalline nanostructures including nanocrystals, nanocubes, nanorods, nanowires, nanotubes, hollow structures, nanoflakes, nanofibers, and so on, have been fabricated through different techniques, such as chemical vapour deposition, hydrothermal synthesis [12], sonochemical technique, chemical precipitation [13], sol-gel technique [14], microemulsion technique [15], hydrolysis [16] ball milling [17], laser ablation, sputtering, and spray pyrolysis [18].

Since most of these reported methods either demand sophisticated instrumentation or require elevated temperature, the preparation of α-Fe$_2$O$_3$ NPs at low cost at the industrial scale is a challenge. Therefore, using the cheap starting materials, simple fabrication processes and suitable conditions of synthesis are the main requirement for low cost/facile synthesis procedures. In this context, it is practically significant to obtain α-Fe$_2$O$_3$ NPs using a facile, cheap, and effective way such as Pechini sol-gel method. Pechini *et al.* [19] introduced a polymerizable complex route, referred to as Pechini method, to serve as an important supplement for the conventional sol-gel method and due to its cheapness, handiness, good stoichiometric control, low toxicity, low cost and insensitivity to water existence, this method has been used rather extensively in synthesis of

*Corresponding author: tel: +9837131984,
fax: +9837131984, e-mail: alisonmirzaee@yahoo.com*

different materials. Moreover the highly branched polymer can reduce the cation mobility during heat treatment, so that the product with a good dispersion could be prepared [20]. In a typical Pechini process, common metal salts are dissolved in a solution using an α-hydroxy carboxylic acid, such as citric acid (CA) as chelating agents of metal ions, then a poly hydroxyl alcohol, such as ethylene glycol (EG) or polyethylene glycol (PEG) is introduced as a crosslinking agent to form a polymeric resin on molecular level, thus, segregation of particular metal ions is reduced and compositional homogeneity is guaranteed.

The goal of this work is to synthesize mesoporous iron oxide by a Pechini route using iron nitrate as precursor, citric acid as chelating agent and ethylene glycol as crossing-linking agent. Afterwards, the aim is to fully characterize synthesized powders using different techniques and finally to study electrical properties and effect of UV light on the electrical resistance of mesoporous α-Fe$_2$O$_3$ NPs.

II. Experimental

2.1. Synthesis of α-Fe$_2$O$_3$ NPs

Hydrated iron nitrate (Fe(NO$_3$)$_3$×9 H$_2$O), citric acid (C$_6$H$_8$O$_7$×H$_2$O), poly(vinyl pyrrolidone) and ethylene glycol (C$_2$H$_6$O$_2$) were purchased from Merck. All the chemicals were used as received and without further purification. Double distilled water was used to prepare precursor solutions. First, Fe(NO$_3$)$_3$×9 H$_2$O was dissolved in distilled water at 70 °C for 1 h under magnetic stirring to make 0.5 M Fe^{+3} solution. In a separate beaker citric acid (CA) was dissolved in distilled water at 70 °C for 30 min. Subsequently, the CA solution was added slowly to the Fe^{+3} solution with stirring ([CA]/[Fe^{+3}] = 2). Then the esterification agent, i.e. ethylene glycol (EG), was added with a molar ratio [CA]/[EG] = 2, while stirring and heating the solution. The final solution was reflux at 120 °C for 2 h. The generated precursor resin was dried at 120 °C for 12 h to obtain the precursor powders. Finally, the amorphous powders were calcined at 550 °C in air atmosphere for 3 h using a muffle furnace to obtain iron oxide NPs.

2.2. Characterization of synthetized nanopowders

Characterization of α-Fe$_2$O$_3$ NPs was achieved by different techniques. X-ray diffraction analysis (XRD) was performed using Philips X-Pert diffractometer operating with monochromatic CuKα (λ = 1.54056 Å) radiation at 40 kV and 30 mA. The XRD pattern was recorded at room temperature at a scan rate 0.05°/sec and 2θ from 10° to 70°. Morphological analysis was carried out using scanning electron microscopy (SEM) by using JEOL 5600 LV instrument operating with a 20 kV accelerating voltage and equipped with EDS detector (Oxford instruments). Morphological studies of synthesized powders were performed with JEOL JEM 2010 electron microscope (LaB$_6$ electron gun) operat-

ing at 200 kV and equipped with Gatan 794 Multi-Scan CCD camera. Room-temperature micro-Raman spectroscopy (μRS) was used to get information about the material quality, the phase and purity. Raman spectrum was recorded at room temperature using micro-Raman spectrometer (Renishaw, Great Britain) in the back scattering geometry with 514.5 nm Ar$^+$ laser as an excitation source and data were collected in the range of 150–1550 cm^{-1}. The molecular structure of iron oxide NPs was studied by using Fourier transform infrared spectrometer (Nicolet FTIR Impact 400D), with the frequency ranging from 400–3500 cm^{-1}. Optical absorbance of iron oxide was recorded with a 1 cm path length quartz cell using a UV-Vis spectrophotometer as a function of wavelength in the range from 200 to 800 nm. X-ray photoelectron spectroscopy (XPS) was employed to determine the surface component and composition of the prepared nanoparticles. XPS was performed on ESCALAB MKII X-ray photoelectron spectrometer (VG Instruments, CA, USA), using non-monochromatized Mg-Kα X-rays as the excitation source. The binding energies for the samples were calibrated by setting the measured binding energy of C1s to 284.60 eV. Thermal analysis was carried out on Mettler Toledo thermal gravimetric analyser and Perkin Elmer differential thermal analyser. The analysis was performed in air flow, in the temperature range between 25 and 600 °C, with heating rate of 10 °C/min. Brunauer-Emmett-Teller (BET) surface area and pore size distribution of the samples were measured by nitrogen adsorption-desorption analyser (Quantachrome Autosorb-1C). All the particles were degassed under vacuum at 150 °C for 2 h before the measurements, and the nitrogen gas adsorption at 77 K was measured using a continuous flow method with nitrogen and helium mixture as the carrier gas. Specific surface area (SBET) was calculated by using the BET method, and pore size distribution was determined by applying the Barrett-Joyne-Halenda (BJH) model.

2.3. Electrical measurements

For electrical measurements, α-Fe$_2$O$_3$ thick films were prepared by drop cast method on the Pt-electroded alumina substrate equipped with Pt heater and electrical resistance was studied by means of Agilent 34970A multimeter using the two point method.

III. Results and discussion

3.1. Mechanisms in Pechini sol-gel preparation

The Pechini method used in the present work allowed obtaining of the homogeneous metal-organic polymer in which the iron ions were randomly distributed along the backbone of the polymer. During the heat treatment at 120 °C, this polymeric precursor method goes through two main stages: the first one is the reaction mechanism of esterification of citric acid with ethylene glycol as indicated in Fig. 1a, and the second one, the chelation of

the iron nitrate by the formed esters as shown in Fig. 1b. Citric acid and ethylene glycol generate a reaction of esterification, and the formed ester acts as complexing agent of the iron cations forming a polymer network that is resin-like or solid as viscosity increases. At this point, it is necessary for the exchange reaction of the iron nitrate with the acid group to proceed until its completion. If this exchange reaction is not driven to completion, precipitation of unreacted iron nitrate would occur in the resin on cooling and this may lead to gross segregation of the iron in the ceramic. In the considered system, the polymer solidified to a clear resin on cooling, implying that all of the iron nitrate had reacted with the polymer [21]. Figure 2 shows Fe^{+3}-citric acid complex and polyesterification process.

3.2. Structural and morphological studies

Figure 3 shows thermo-gravimetric (TGA) and differential thermal analysis (DTA) of the dried iron oxide gel. According to TGA curve of amorphous iron oxide, decomposition proceeds with thermal treatment through three steps. Initially, at a temperature below 100 °C, a small weight loss is observed, probably due to the evaporation of humidity adsorbed during storage is observed. Two other large weight losses are observed at temperatures higher than 150 °C, starting at about 185 and 250 °C, respectively. These are due to the decomposition of organic species from citric acid and ethylene glycol. No further weight loss is observed above 350 °C, thus indicating that the organic material was completely
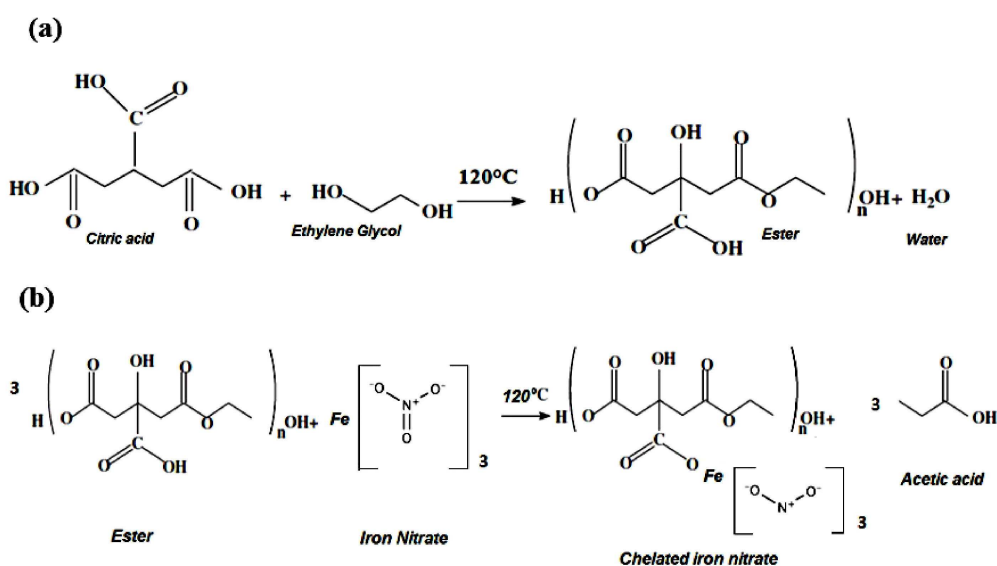

Figure 1. Reaction mechanism for esterification of citric acid with ethylene glycol (a) [21] and reaction mechanism of chelation of iron nitrate by polymer (b)
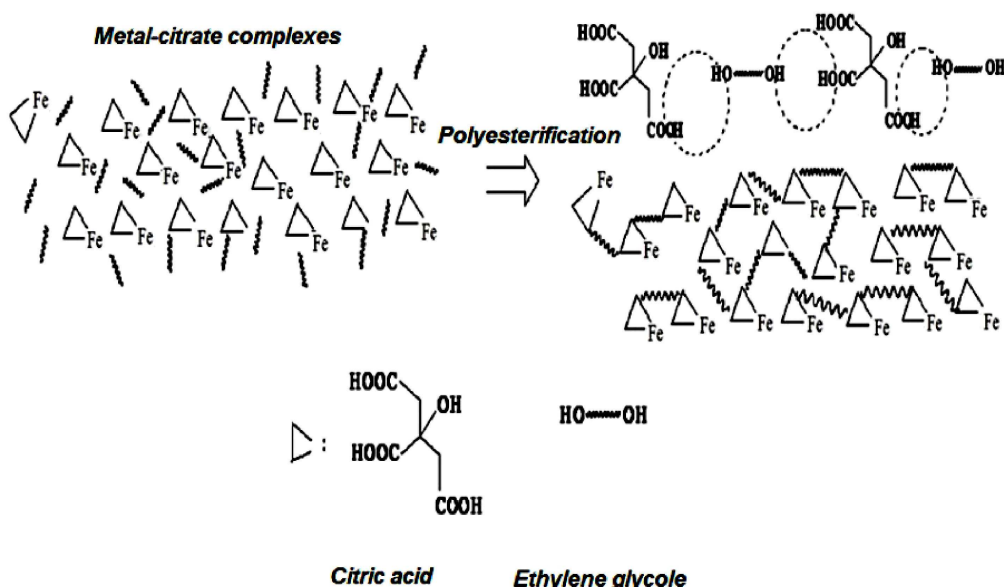

Figure 2. Chelating process (formation of metal citrate complexes) and polyesterification during Pechini process [22]
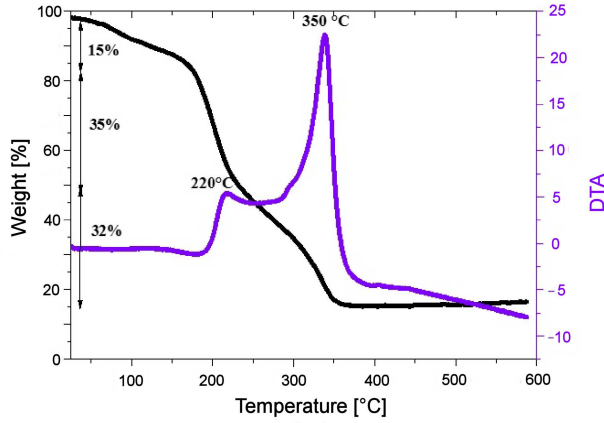
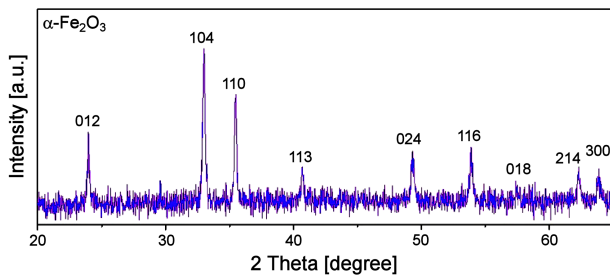**Figure 3. TGA/DTA curves of amorphous iron oxide**

Figure 4. X-ray diffraction pattern of α-Fe$_2$O$_3$ NPs

eliminated at this temperature. DTA profile shows two peaks which are associated with exothermic reactions. On the basis of these experimental evidences and literature data, the peak at 220 °C is related to the transformation of amorphous phase to crystalline γ-Fe$_2$O$_3$, whereas the second peak at 350 °C is likely attributed to its transformation to α-Fe$_2$O$_3$ [23].

Figure 4 shows the XRD pattern of the calcined iron oxide powder. All the diffraction peaks can be assigned to the hexagonal α-Fe$_2$O$_3$ phase and are consistent with those reported in the literature and with the respective JCPDS card no. 89-596.

The lattice constants a and c of α-Fe$_2$O$_3$ were evaluated according to Bragg law:

$$n \cdot \lambda = 2d \cdot \sin\theta \tag{1}$$

where n is the order of diffraction, λ is the X-ray wavelength, and d is the spacing between planes of given Miller indices h, k, and l. In the hexagonal structure of α-Fe$_2$O$_3$, the plane spacing is related to the lattice constant a, c, and Miller indices by the following formulas:

$$\left(\frac{1}{d}\right)^2 = \frac{4}{3}\left(\frac{h^2 + hk + k^2}{a^2}\right) + \left(\frac{l}{c}\right)^2 \tag{2}$$

$$\sin^2\theta = \frac{\lambda^2}{4}\left[\frac{4}{3}\left(\frac{h^2 + hk + k^2}{a^2}\right) + \left(\frac{l}{c}\right)^2\right] \tag{3}$$

According to the above formulas, for the (110) plane with diffraction peak at $2\theta = 35.64°$, the lattice constant a was calculated by:

$$a = \frac{\lambda}{\sin\theta} \tag{4}$$

and for (104) plane with diffraction peak at $2\theta = 33.15°$, the lattice constant c was calculated by:

$$c = \sqrt{\frac{12a^2 \cdot \lambda^2}{3a^2 \sin^2\theta - \lambda^2}} \tag{5}$$

The lattice parameters for the hexagonal phase of α-Fe$_2$O$_3$ using Eq. (5) have been calculated to be $a = 0.50$ nm and $c = 1.39$ nm, which are in close agreement with the reported data.

Figure 5a shows TEM micrograph of iron oxide powder calcined at 550 °C for 3 h. Very fine particles with sizes between 10–30 nm are observed. Figure 5b shows SEM micrograph of α-Fe$_2$O$_3$ thick film on the alumina substrate. As clearly observed, it has quite porous structure that renders a high surface area for these particles. Porous structure is the result of the burning of polymeric species from ethylene glycol.
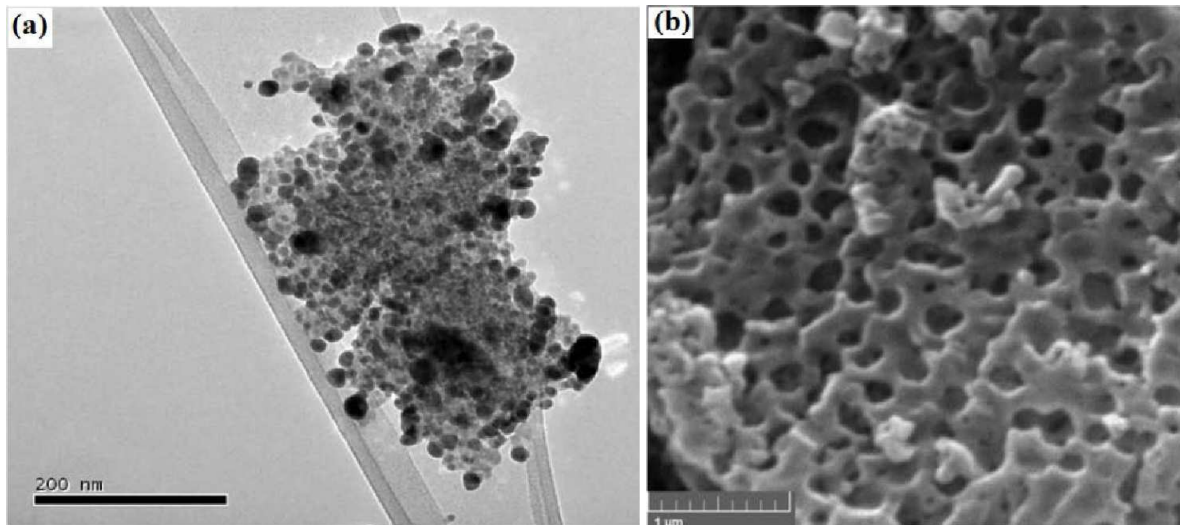

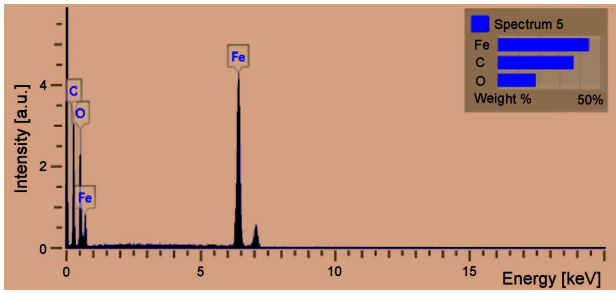**Figure 5. TEM (a) and SEM (b) micrographs of iron oxide NPs calcined at 550 °C for 3 h**

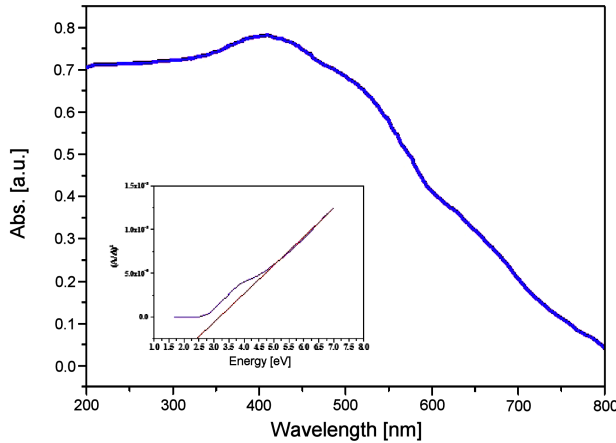**Figure 6. EDS analysis of iron oxide sample 550 °C for 3 h**

Figure 7. UV-Vis spectrum of α-Fe$_2$O$_3$ NPs. (inset) Tauc plot of α-Fe$_2$O$_3$ NPs
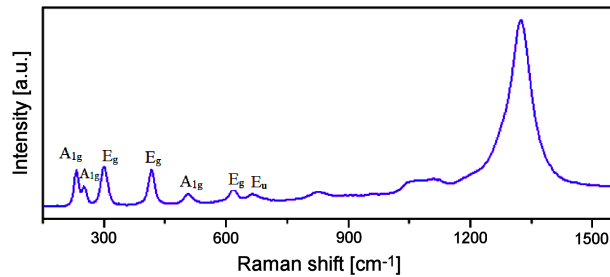

Figure 8. Raman spectrum of α-Fe$_2$O$_3$ NPs

Figure 6 shows EDS analysis of iron oxide calcined at 550 °C for 3 h. It reveals the presence of O and Fe elements and no significant signals of other elements from starting materials, which indicates that the synthesized iron oxides are pure.

The UV-Vis spectrum of the calcined α-Fe$_2$O$_3$ NPs is presented in Fig. 7. For recording of UV-Vis spectra, the sample of α-Fe$_2$O$_3$ solution was prepared in absolute ethanol dispersed by ultrasonic bath. The absorption peak in Fig. 7 corresponds to α-Fe$_2$O$_3$ nanopowders showing the strong absorption in the wavelength of ~400 nm.

From these spectral data, the absorption coefficient was calculated using the following relationship [24]:

$$\alpha \cdot h \cdot v = A \left(h \cdot v - E_g^{Opt} \right)^m \quad (6)$$

where α is absorption coefficient, A is an energy-

independent constant, m is a constant which determines type of the optical transition ($m = 1/2$ for allowed direct transitions and $m = 2$ for allowed indirect transitions) and E_g^{Opt} is the optical band gap. It is evaluated that the optical band gap of the α-Fe$_2$O$_3$ has a direct optical transition. The optical band gap (E_g^{Opt}) could be obtained by the extrapolating method using the $(\alpha \cdot h \cdot v)^{1/2}$ vs. $h \cdot v$ plot. Inset in Fig. 7 shows plot of $(\alpha \cdot h \cdot v)^{1/2}$ vs. $h \cdot v$ for the α-Fe$_2$O$_3$. Value of E_g^{Opt} obtained by this method is 2.4 eV.

The Raman spectroscopy technique has been extensively used for structure, composition, and phase characterization of materials [25]. A Raman analysis was also carried out. α-Fe$_2$O$_3$ belongs to the crystal space group D_{3d}^6. Since the primitive cell contains six atoms, there are 18 modes of vibration divided into 15 optical mode and 3 acoustic modes. According to the group theory of hematite, the following normal vibrational modes are predicted and represented by the hematite's irreducible vibrational mode at the first Brillouin zone centre [26]:

$$\Gamma_{vib} = 2A_{1g} \oplus 2A_{1u} \oplus 3A_{2g} \oplus 2A_{2u} \oplus 5E_g \oplus 4E_u \quad (7)$$

The acoustic $2A_{1u}$ and $2A_{2u}$ modes are optically silent because they are inactive in Raman. As for the optical modes, they are $2A_{1g}$, $5E_g$, $3A_{2g}$, $4E_u$, in which the $2A_{1g}$, $5E_g$ modes are active in Raman and the $3A_{2g}$, $4E_u$ modes are inactive [27]. So it has seven characteristics Raman-active vibrations. The Raman spectrum of the sample is given in Fig. 9. This spectrum exhibit seven spectral signatures that are indicative for hematite, and do not contain any peaks associated with any maghemite.

Figure 8 shows characteristic bands of hematite which can be assigned to $2A_{1g}$ (222 and 498 cm^{-1}) and $5E_g$ (243, 290, 408 and 608 cm^{-1}). Besides the typical $2A_{1g}$ and $5E_g$ symmetry phonon modes (below 620 cm^{-1}), a very strong feature at 1315 cm^{-1} and a very weak peak at 657 cm^{-1} are detected. Hematite is an antiferromagnetic material and the collective spin movement can be excited in what is called a magnon. The intense feature at 1315 cm^{-1} is assigned to a two-magnon scattering which arises from the interaction of two magnons created on antiparallel close spin sites. The peak at 657 cm^{-1}, which is typical of nanocrystalline hematite, originates from the presence of surface defects and/or reduced grain size [28,29].

This result confirms that the calcined product is α-Fe$_2$O$_3$. No other iron oxides such as magnetite or maghemite were detected indicating high purity of the final product. Also the large line widths and the low wave number shifts of the Raman peaks could be due to the phonon confinement effects in the nanocrystals.

To obtain further information about surface area and the distribution of pores in the NPs, BET N$_2$ adsorption-desorption analysis was performed. The adsorption-desorption isotherm and the corresponding BJH pore size distribution plot (inset) of the α-Fe$_2$O$_3$ NPs are

shown in Fig. 9. According to the IUPAC classification, the loop observed is ascribed to type H3 loops and the BET surface area of the material was calculated to be ~30 m^2/g. BJH plot indicates the existence of mesopores (pores 2–50 nm in diameter) in the α-Fe_2O_3 NPs. The size of mesopores in the architecture was not uniform and most of the pores fall into a size range from 5 to 30 nm in diameter.
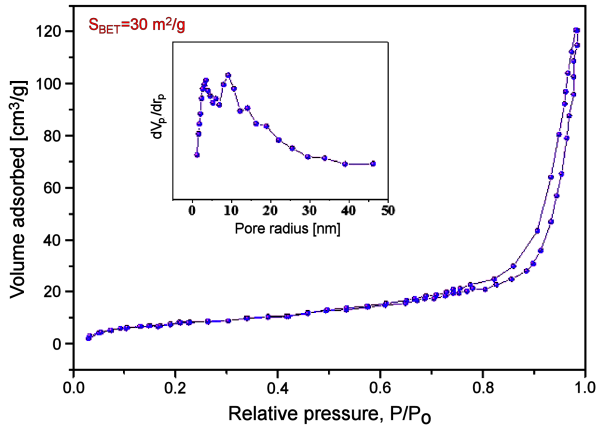

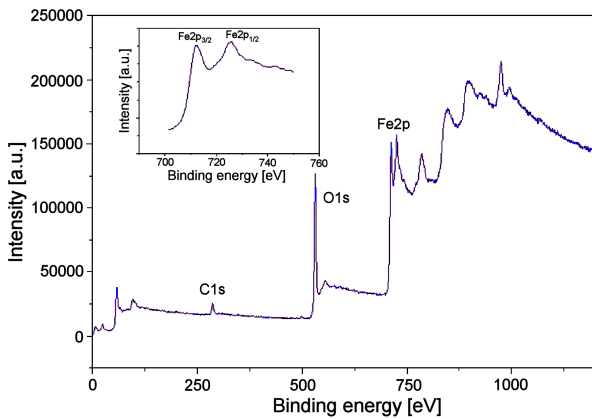**Figure 9. BET curve of Fe₂O₃ NPs. (inset) BJH plot showing distribution of pores**
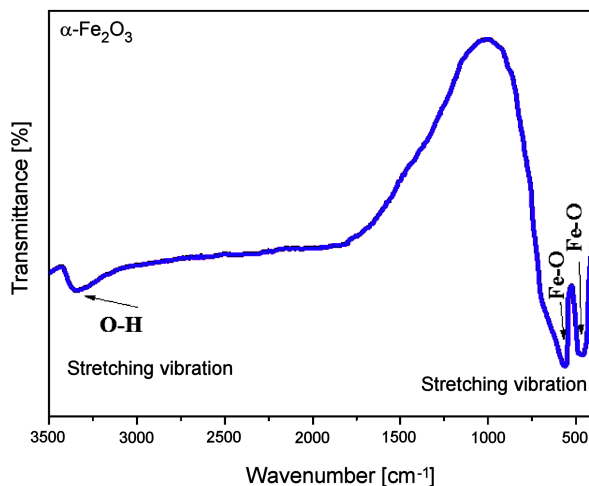

Figure 10. XPS survey of Fe₂O₃ NPs 550 °C/3 h

Figure 11. FTIR spectrum of α-Fe₂O₃ calcined at 550 °C/3 h

The primary difference between the EDS and XPS techniques is that EDS could be used to determine the composition of several different particles individually, then an average could be taken of the composition, while for XPS which is a surface sensitive technique (it can only detect the element no more than 10 nm in the depth [30]), a relatively large analysis area results in simultaneous analysis of several particles.

Figure 10 shows survey of XPS spectrum of calcined (550 °C/3 h) iron oxide. It shows the presence of Fe and O elements. The peak observed at 711.1 eV is attributed to Fe $2p_{3/2}$ and the peak at 725.08 eV is attributed to Fe $2p_{1/2}$. The shake-up satellite line is characteristic of Fe^{+3} in Fe_2O_3. The Fe $2p$ spectra of α-Fe_2O_3 and γ-Fe_2O_3 are almost identical with each other. In both cases, the main peaks maximum of $2p_{3/2}$ and $2p_{1/2}$ have the shake-up structures at their higher binding energy side at about 8.0 eV. In the present case, this value is found to be ~8.0 eV, which confirms the formation of Fe(III) oxide. However, the marked difference in these XPS spectra is that the binding energy of the main peak, $2p_{3/2}$ is slightly higher in the case of α-Fe_2O_3 (711.3 eV) compared to γ-Fe_2O_3 (710.7 eV) [31]. Also appearance of Fe^{+3} cations (711.1 eV) rather than Fe^{+2} cations (709 eV) indicates the presence of the Fe_2O_3 phase [32].

The FTIR spectroscopy was utilized to detect the presence of functional groups adsorbed on the surface of the synthesized α-Fe_2O_3 particles. Figure 11 shows the FTIR spectrum of α-Fe_2O_3 powder acquired from Pechini sol-gel route calcined at 550 °C for 3 h. The band at ~3350 cm^{-1} is assigned to the stretching vibration of water, indicating the existence of a little water absorbed on the sample. Two absorption bands below 1000 cm^{-1} represent characteristic features of α-Fe_2O_3 and are assigned to metal oxygen stretching frequencies. The high frequency band ~560 cm^{-1} refers to Fe–O deformation in the octahedral and tetrahedral sites while the low frequency band ~462 cm^{-1} is attributed to Fe–O deformation in the octahedral site of hematite [31]. The intensity of absorption band at 560 cm^{-1} is stronger than that at 462 cm^{-1}. It gives further evidence for the formation of α-Fe_2O_3 and this is in agreement with the XRD measurement. There is no peak at 2900 cm^{-1} indicating the C–H stretching band, which means all organic compounds are removed from the samples after calcinations at 550 °C.

The DC electrical resistivity of the iron oxide thick film was measured as a function of temperature in the range of 483–673 K using DC two-probe method. Because resistance of the film at room temperature was very high and exceeds the limit of the used instrument (120 MΩ), it could not be measured using the experimental setup. However at higher temperatures, the resistance fall within readable value, and the electrical properties of α-Fe_2O_3 NPs were evaluated in dry air in the range of 483–673 K. Figure 12 shows electrical resistance change of the sensor during heating and cooling
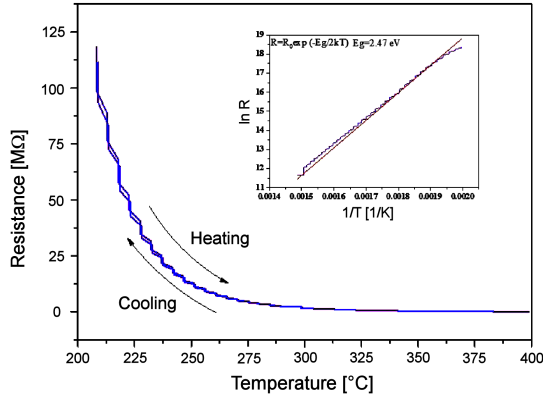
214

Figure 12. Heating-cooling curves showing electrical resistance of α-Fe$_2$O$_3$ NPs as a function of temperature (inset - variations of $\ln R$ versus $(1/T)$ for the α-Fe$_2$O$_3$ NPs)

cycles. As it clearly could be seen, resistance of sensor on heating and cooling is approximately the same. This means that sensor resistance is very stable upon heating and cooling cycles. The relationship between the resistance and temperature is as follows:

$$R_T = R_0 \exp\left(\frac{E_g}{2k \cdot T}\right) \tag{8}$$

where R_0 is the pre-exponential factor, k is the Boltzmann's constant, E_g is bulk electrical band gap. From the plot of $\ln R$ against $1/T$ the band bending of the sensing layer can be determined. The plot of resistance versus inverse temperature, shown in inset of Fig. 12, shows that the temperature dependent resistance values obey the Arrhenius relation (a linear trend) and a linear decrease of the $\ln R_T$ with increase in the temperature is observed. The estimated value of electrical band gap was found to be $\sim$2.47 eV. It is worthy to note that for individual particles, there is a relationship between electrical band gap ($E_g^{El} = E_g^{bulk,el} + E_{ee}$) and optical band gap ($E_g^{Opt} = E_g^{bulk,el} + E_{ee} - E_{eh}$, where E_{ee} and E_{eh} are the electron-electron and electron-hole interaction energies, respectively [33]). However, for most inorganic semiconductors the values of E_g^{El} and E_g^{Opt} of particles are almost the same.

After heating to high temperatures, the resistance decreased strongly. The resistance of a layer with length l and cross section A is defined as:

$$R = \rho \frac{l}{A} \tag{9}$$

where ρ is the resistivity of the layer. Conductivity (inverse function of resistivity, $\sigma = 1/\rho$) can be expressed by the product of the charge q, the effective mobility μ of the layer and the electron concentration n_b:

$$\sigma = q \cdot \mu \cdot n_b \tag{10}$$

Combining the latter three expressions one obtains:

$$R = \frac{l}{q \cdot \mu \cdot n_b \cdot A} \tag{11}$$

Thus, for a given material with constant l and A, if n_b increases R will decrease. For semiconductor materials, there is an exponential relationship between n_b and temperature:

$$n_b = \sqrt{N_c \cdot N_v} \exp\left(-\frac{E_g}{2k \cdot T}\right) \tag{12}$$

where N_c and N_v are the effective density of states in the conduction band and valence band, respectively. According to above equation as temperature increases, n_b will increase. In case of α-Fe$_2$O$_3$ as a semiconductor, with increase of temperature more electrons transfer to conduction band and consequently n_b increases and the resistance will decrease [34]. It is worthy to note that as Fe$_2$O$_3$ is a narrow band gap semiconductor and mobility of ions at tested temperatures are much lower than the mobility of electrons and it is supposed that electrical conductivity is dominant in this material [35].

Temperature coefficient $\alpha(T)$ can be written as follow [36]:

$$\alpha(T) = \frac{1}{R}\frac{dR}{dT} \tag{13}$$

If temperature change is not significant as in our case, it can approximately be written as:

$$\Delta R = \alpha \cdot R \cdot \Delta T \tag{14a}$$

or

$$\alpha = \frac{1}{R}\frac{\Delta R}{\Delta T} = \frac{1}{R}\frac{R_{T_2} - R_{T_1}}{T_2 - T_1} \tag{14b}$$

The variation of the electrical resistance as a function of the temperature was characterized by a negative temperature coefficient of electrical resistance. As with increase of temperature the resistance decreases, so α has a negative value, which is consistent with a semiconducting-type behaviour.

Figure 13 shows a schematic diagram of the photo-excitation in semiconductors. When UV radiation falls on the metal oxide, the absorption of a photon with enough energy promotes an electron in conduction band and it generates a hole in the valence band; the photo-generated holes recombine with electrons trapped on the surface causing desorption of the adsorbed oxygen ions. This results in the conductivity increase due to the increased free electrons density.

The required energy for band to band excitation depends on the band gap energy of semiconductors. According to band gap determined from Tauc plot band gap of α-Fe$_2$O$_3$ NPs was about $\sim$2.4 eV. The photon energy is determined by light wavelength ($E = h \cdot c/\lambda$). This means that the photon energy of 400 nm (3.1 eV) is sufficient for band to band excitation of α-Fe$_2$O$_3$ NPs. Figure 14 shows effect of UV light on the resistance change of α-Fe$_2$O$_3$ NPs. As it can be observed, UV light has little effect on the resistance of α-Fe$_2$O$_3$ NPs. Before UV light irradiation, large amount of O$_2^-$ is absorbed on
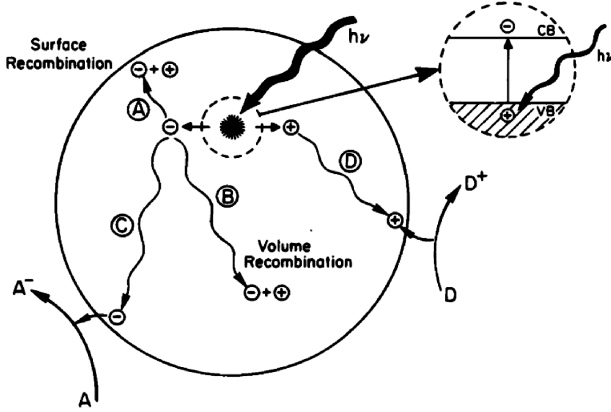
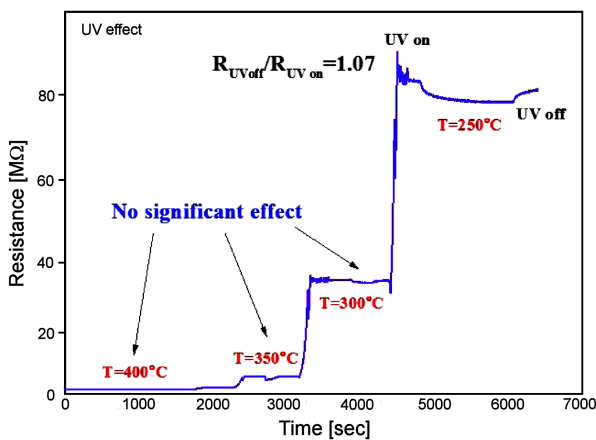**Figure 13. Schematic representation of the photo-excitation in semiconductors [37]**

Figure 14. Effect of UV light on resistance of α-Fe$_2$O$_3$ NPs

the surface of the α-Fe$_2$O$_3$ NPs, which induced the formation of depletion layer. Upon UV irradiation, photo generated holes and electrons appeared, and then they are separated under the effect of the built-in electric fields. Due to the built-in electric fields, electrons migrated inside of the particles while the holes remained on the surfaces or migrated to the surfaces and reacted with O_2^-, which induced the desorption of O_2 [38]:

$$h^+(h\nu) + O_2^-{}_{(ads)} \rightarrow O_{2(g)} \qquad (15)$$
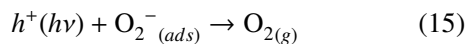
As a result of this reaction oxygen species are photo-desorbed from the surface (decrease of resistance). On the other hand, the photo-generated electrons will also contribute to a decrease of resistance. Little effect of UV light on the final resistance of α-Fe$_2$O$_3$ NPs is probably due to the limited number of extrinsic electrons in α-Fe$_2$O$_3$ NPs.

IV. Conclusions

In this study, α-Fe$_2$O$_3$ nanoparticles (NPs) were successfully synthesized by Pechini sol-gel method and were fully characterized by different techniques. TEM results confirmed the formation of ultrafine NPs and results of XRD and TGA/DTA demonstrated the forma-

tion of hematite at 550 °C. Also XPS, FTIR and EDS results proved the formation of desired chemical composition and purity of synthesized NPs. Furthermore BET results showed a high surface area which originated from nanosize nature of synthesized NPs. Thick films of Fe$_2$O$_3$ NPs prepared on the interdigitated alumina substrates and the electrical resistances at different temperatures were studied. It was found that the prepared α-Fe$_2$O$_3$ thick films had very stable electrical properties which are especially good for gas sensing applications. Moreover, the effect of UV light on the electrical resistance of sensor was studied and it was found that UV light had no significant effect on the change of electrical resistance of Fe$_2$O$_3$ thick films.

References

1. A. Mirzaei, B. Hashemi, K. Janghorban, "α-Fe$_2$O$_3$ based nanomaterials as gas sensors", *J. Mater. Sci.: Mater. Electron.*, **27** (2016) 3109–3144.
2. H. Shan, C. Liu, L. Liua, S. Li, L. Wang, X. Zhang, X. Bo, X. Chia, "Highly sensitive acetone sensors based on La-doped α-Fe$_2$O$_3$ nanotubes", *Sensors Actuators B: Chem.*, **184** (2013) 243–247.
3. Y. Sun, G. Guo, B. Yang, W. Cai, Y. Tian, M. He, Y. Liu, "One-step solution synthesis of Fe$_2$O$_3$ nanoparticles at low temperature", *Physica B*, **406** (2011) 1013–1016.
4. X.L. Fang, C. Chen, M.S. Jin, Q. Kuang, Z.X. Xie, S.Y. Xie, R.B. Huang, L.S. Zheng, "Single-crystal-like hematite colloidal nanocrystal clusters: synthesis and applications in gas sensors, photocatalysis and water treatment", *J. Mater. Chem.*, **19** (2009) 6154–6160.
5. A.K. Gupta, M. Gupta, "Synthesis and surface engineering of iron oxide nanoparticles for biomedical applications", *Biomater.*, **26** (2005) 3995–4021.
6. A. Mirzaei, K. Janghorban, B. Hashemi, A. Bonavita, M. Bonyani, S.G. Leonardi, G. Neri, "Synthesis, characterization and gas sensing properties of Ag@α-Fe$_2$O$_3$ core-shell nanocomposites", *Nanomater.*, **5** (2015) 737–749.
7. G. Neri, A. Bonavita, S. Galvagno, P. Siciliano, S. Capone, "CO and NO$_2$ sensing properties of doped-Fe$_2$O$_3$ thin films prepared by LPD", *Sens. Actuators B: Chem.*, **82** (2002) 40–47.
8. S. Mitra, S. Das, K. Mandal, S. Chuadhari, "Synthesis of a-Fe$_2$O$_3$ nanocrystal in its different morphological attributes: Growth mechanism, optical and magnetic properties", *Nanotechnol.*, **18** (2007) 275608.
9. Z.Y. Fan, X.G. Wen, S.H. Yang, J.G. Lu, "Controlled p-and n-type doping of Fe$_2$O$_3$ nanobelt field effect transistors", *Appl. Phys. Lett.*, **87** (2005) 013113.
10. S. Wagloehner, D. Reichert, D.L. Sorzano, P. Balle, B. Geiger, S. Kureti, "Kinetic modeling of the oxidation of CO on Fe$_2$O$_3$ catalyst in excess of O$_2$", *J.*

Catal., **260** (2008) 305–314.

11. N. Pailhé, A. Wattiaux, M. Gaudon, A. Demourgues, "Impact of structural features on pigment properties of α-Fe$_2$O$_3$ haematite", *J. Solid State Chem.*, **181** (2008) 2697–2704.

12. C.Q. Hu , Z.H. Gao , X.R. Yang, "Facile synthesis of single crystalline α-Fe$_2$O$_3$ ellipsoidal nanoparticles and its catalytic performance for removal of carbon monoxide", *Mater. Chem. Phys.*, **104** (2007) 429–433.

13. H. Asnaashari Eivari, A. Rahdar, "Some properties of iron oxide nanoparticles synthesized in different conditions", *World Appl. Program.*, **3** (2013) 52–55.

14. D.K. Bandgar, S.T. Navale, G.D. Khuspe, S.A. Pawar, R.N. Mulik, V.B. Patil, "Novel route for fabrication of nanostructured α-Fe$_2$O$_3$ gas sensor", *Mater. Sci. Semicond. Process.*, **17** (2014) 67–73.

15. R. Ramesh, K. Ashok, G.M. Bhalero, S. Ponnusamy, C. Muthamizhchelvan, "Synthesis and properties of α-Fe$_2$O$_3$ nanorods", *Cryst. Res. Technol.*, **45** (2010) 965–968.

16. H. Yan, X. Su, C. Yang, J. Wang, C. Niu, "Improved photocatalytic and gas sensing properties of α-Fe$_2$O$_3$ nanoparticles derived from β-FeOOH nanospindles", *Ceram. Int.*, **40** (2014) 1729–1733.

17. M.H. Mahmound, H.H. Hamdeh, J.C. Ho, M.J. O'Shea, J.C. Walker, "Mössbauer studies of manganese ferrite fine particles processed by ball-milling", *J. Magn. Magn. Mater.*, **220** (2000), 139–146.

18. S.S. Shinde, A.V. Moholkar, J.H. Kim, K.Y. Rajpure, "Structural, morphological, luminescent and electronic properties of sprayed aluminium incorporated iron oxide thin films", *Surface Coatings Technol.*, **205** (2011) 3567–3577.

19. M.P. Pechini, U.S Patent, No 3.330.697, 1967.

20. Y. Wu, X. Wang, "Preparation and characterization of single-phase α-Fe$_2$O$_3$ nano-powders by Pechini sol-gel method", *Mater. Lett.*, **65** (2011) 2062–2065.

21. C. Sanchez, J. Doria, C.Paucar, M. Hernandez, A. Mosquera, J.E. Rodrıguez, A. Gomez, E. Baca, O. Moran, "Nanocystalline ZnO films prepared via polymeric precursor method (Pechini)", *Physica B: Condensed Matter*, **405** (2010) 3679–3684.

22. J. Lin, M. Yu, C. Lin, X. Liu, "Multiform oxide optical materials via the versatile pechini-type sol-gel process: synthesis and characteristics", *J. Phys. Chem. C*, **111** (2007) 5835–5845.

23. G. Picasso, M.R.S. Kou, O. Vargasmachuca, J. Rojas, C. Zavala, A. Lopez, S. Irusta, "Sensors based on porous Pd-doped hematite (a-Fe$_2$O$_3$) for LPG detection", *Micropor. Mesopor. Mater.*, **185** (2014) 79–85.

24. M.A.M. Khana, S. Kumar, M. Ahameda, S.A. Alrokayana, M.S. Alsalhi, M. Alhoshana, A.S. Aldwayyana, "Structural and spectroscopic studies of thin film of silver nanoparticles", *Appl. Surface Sci.*, **257** (2011) 10607–10612.

25. K.P. Jayadevan, T.Y. Tseng, "Oxide nanoparticles", *Chem. Inform.*, **36** (2005) 335–336.

26. S. Babay, T. Mhiri, M. Toumi, "Synthesis, structural and spectroscopic characterizations of maghemite α-Fe$_2$O$_3$ prepared by one-step coprecipitation route", *J. Mol. Struct.*, **1085** (2015) 286–293.

27. D.L.A. De Faria, S.V. Silva, M.T. De Oliveira, "Raman microspectroscopy of some iron oxides and oxyhydroxides", *J. Raman Spectro.*, **28** (1997) 873–878.

28. I. Cesar, K. Sivula, A. Kay, R. Zboril, M. Grzel, "Influence of feature size, film thickness, and silicon doping on the performance of nanostructured hematite photoanodes for solar water splitting", *J. Phys. Chem. C*, **113** (2008) 772–782.

29. S.H. Shim, T.S. Duffy, "Raman spectroscopy of Fe$_2$O$_3$ to 62 GPa", *Am. Mineral.*, **87** (2002) 318–326.

30. D. Huo, J. He, H. Li, H. Yu, T. Shi, Y. Feng, Z. Zhou,Y. Hu, "Fabrication of Au@Ag core-shell NPs as enhanced CT contrast agents with broad antibacterial properties", *Colloids Surfaces B: Biointerfaces*, **117** (2014) 29–35.

31. G. Wu, X. Tan, G. Li, C. Hu, "Effect of preparation method on the physical and catalytic property of nanocrystalline Fe$_2$O$_3$", *J. Alloys Compd.*, **504** (2010) 371–376.

32. M.A. Bhosale, D. Ummineni, T. Sasaki, D.N. Hamaned, B.M. Bhanage, "Magnetically separable γ-Fe$_2$O$_3$ nanoparticles: An efficient catalyst for acylation of alcohols, phenols, and amines using sonication energy under solvent free condition", *J. Mol. Catal. A: Chem.*, **404** (2015) 8–17.

33. A. Majumdar, R. Bogdanowicz, S. Mukherjee, R. Hippler, "Role of nitrogen in optical and electrical band gaps of hydrogenated/hydrogen free carbon nitride film", *Thin Solid Films*, **527** (2013) 151–157.

34. M. Hübner, N. Bârsan, U. Weimar, "Influences of Al, Pd and Pt additives on the conduction mechanism as well as the surface and bulk properties of SnO$_2$ based polycrystalline thick film gas sensors", *Sensors Actuators B*, **171-172** (2012) 172–180.

35. C.B. Carter, M.G. Norton, *Ceramic Materials: Science and Engineering*, Springer Science & Business Media, 2007.

36. Y.D. Wang, X.H. Wu, Z.L. Zhou, "A new type of semiconductor gas sensor based on the n-n combined structure", *Sensors Actuators B*, **73** (2001) 216–220.

37. M.C. Carotta, A. Cervi, A. Fioravanti, S. Gherardi, A. Giberti, B. Vendemiati, D. Vincenzi, M. Sacerdoti, "A novel ozone detection at room temperature through UV-LED-assisted ZnO thick film sensors", *Thin Solid Films*, **520** (2011) 939–946.

38. S. Park, S. An, Y. Mun, C. Lee, "UV-activated gas sensing properties of ZnS nanorods functionalized with Pd", *Curr. Appl. Phys.*, **14** (2014) S57–S62.